

Magnetism-mediated thermoelectric performance of the Cr-doped bismuth telluride tetradymite

J.-B. Vaney^a, S. Aminorroaya Yamini^{b, c, **}, H. Takaki^d, K. Kobayashi^a, N. Kobayashi^d, T. Mori^{a, d, *}

^a International Center for Materials Nanoarchitectonics (WPI-MANA) and Center for Functional Sensor & Actuator (CFSN), National Institute for Materials Science (NIMS), Tsukuba, 305-0044, Japan

^b Australian Institute for Innovative Materials (AIIM), Innovation Campus, University of Wollongong, North Wollongong, NSW, 2500, Australia

^c Department of Engineering and Mathematics, Sheffield Hallam University, Sheffield, S1 1WB, UK

^d Faculty of Pure and Applied Sciences, University of Tsukuba, Tsukuba, 305-8671, Japan

ARTICLE INFO

Article history:

Received 15 November 2018

Received in revised form

21 March 2019

Accepted 21 March 2019

Available online 2 April 2019

ABSTRACT

Enhancing the efficiency of thermoelectric materials has been practiced extensively by either improving the power factor or reducing the lattice thermal conductivity. Magnetism, and the magnetic moment –charged carrier interactions, has been suggested to enhance the efficiency of some compounds. Nevertheless, decoupling of the magnetic and the carrier concentration–related effects has never been achieved to prove once and for all, the importance of magnetism in thermoelectricity. Herein, we report improved quality criterion of bismuth telluride upon chromium substitution. The magnetic interactions with the magnetic moment carried by Cr atoms have increased the electrons' effective mass, enhancing the thermopower. Combined with the decrease in the lattice thermal conductivity, the overall performance of these compounds has been enhanced by 25% at constant carrier concentration, an improvement seldom observed. This is a robust enhancement principle because magnetic interactions are effective at high temperatures above the transition temperature, unlike magnon drag which is dependent on ordering and typically a low temperature phenomenon. Our results indicate that taking advantage of such relatively easily implemented magnetic doping effects along with existing strategies can lead to enhanced efficiency of thermoelectric materials.

© 2019 The Authors. Published by Elsevier Ltd. This is an open access article under the CC BY license (<http://creativecommons.org/licenses/by/4.0/>).

1. Introduction

Solid-state thermoelectric generators have been increasingly attracting attention in the past decades owing to the need for new technologies for energy conversion [1–3]. Thermoelectric materials convert heat to electricity and vice versa, leading to new systems for waste heat recovery from automobiles and industries or power generations for sensors, and refrigeration. The efficiency of thermoelectric materials is defined by figure of merit, $zT = \frac{S^2}{\rho\kappa}T$, where S , ρ , κ and T are the Seebeck coefficient (thermopower), electrical

resistivity, thermal conductivity and absolute temperature, respectively. The enhancement of zT is, however, challenging due to strong correlation of these physical properties together. Substantial efforts have been devoted to reduce the lattice thermal conductivity of bulk thermoelectric materials by seeking materials with intrinsically low thermal conductivity [4–7] or nanostructuring bulk materials [8–10]. Despite the popularity of bulk nanostructuring in the last decade, the reduction of the lattice thermal conductivity is achieved at the expense of reduced carrier mobility, initiated from scattering of charge carriers [11–13]. Therefore, improving the power factor, $S^2\sigma$, seems to be the most viable strategy to further enhance the efficiency of thermoelectric materials. However, there is a conventional trade-off between S and $1/\rho$. Therefore, enhancement of the power factor has been achieved through engineering the electronic band structure near the Fermi level and tuning the scattering mechanisms, including resonant states [14,15], multiple bands convergence [16–19], manipulating the band gap [20–22] and/or modulation doping [23]. Recently,

* Corresponding author. International Center for Materials Nanoarchitectonics (WPI-MANA) and Center for Functional Sensor & Actuator (CFSN), National Institute for Materials Science (NIMS), Tsukuba, 305-0044, Japan.

** Corresponding author. Department of Engineering and Mathematics, Sheffield Hallam University, Sheffield, S1 1WB, UK.

E-mail addresses: SAminorroaya@shu.ac.uk (S. Aminorroaya Yamini), Mori.Takao@nims.go.jp (T. Mori).

magnetic interactions have also been proposed as a strategy to enhance the thermopower [24–27]. Charge carriers interact with the local magnetic moments, resulting in increased charge carrier effective mass and consequently enhance thermopower. Previous reports have proved beneficial effect of magnetism on the thermoelectric performance of antiferromagnetic CuFeS_2 chalcopyrites [24,25,28] and dilute magnetism of Mn in CuGaTe_2 chalcopyrite [26]. However, to clearly differentiate the magnetism-driven enhancements from charge carrier concentration-driven variations on transport properties of these materials, samples are required to be compared at constant carrier concentration.

Here, we have doped bulk bismuth telluride samples with chromium to obtain n-type dilute magnetic $\text{Bi}_{2-x}\text{Cr}_x\text{Te}_3$ ($0 \leq x \leq 0.1$) compounds and determined their electronic and magnetic properties. Chromium has shown solubility of less than $x = 0.02$ in bismuth telluride. Our results indicate that upon neutral substitution of Cr for Bi (i.e. isovalent substitution of Bi with Cr atoms) in $\text{Bi}_{1.99}\text{Cr}_{0.01}\text{Te}_3$, the power factor is enhanced and the thermal conductivity decreased, leading to an improved zT . Samples of $\text{Bi}_{2-x}\text{Cr}_x\text{Te}_3$ ($0 \leq x \leq 0.01$) with higher carrier concentrations were prepared separately and confirmed these findings. These results differentiate the magnetism-driven enhancement of the power factor from the effects of carrier concentration in diluted magnetic thermoelectric materials and highlight the role of magnetism on the thermoelectric properties.

2. Materials and methods

2.1. Synthesis

Polycrystalline samples of $\text{Bi}_{2-x}\text{Cr}_x\text{Te}_3$ ($x = 0.00, 0.01, 0.02, 0.05$ and 0.10) were synthesized by direct reaction of stoichiometric amounts of high purity (Bi (99.999%, Alfa Aesar) and Te (99.999%, Alfa Aesar) pieces and Cr (99.996%, Alfa Aesar)) powder in vacuum-sealed quartz ampoules, prepared in an Ar glove box. The ampoules were homogenised at 1,323 K for 10 h and quenched in cold water, followed by annealing at 673 K for 3 days.

The obtained ingots were hand-ground into micron-sized powders with agate mortar and pestle in an Ar-atmosphere glove box and consolidated by spark plasma sintering (SPS), Dr. Sinter 8,000 Syntex, at 633 K and an axial pressure of 50 MPa for 5 min under vacuum. The powders were sintered in a graphite die of 10 mm inner diameter with a final height of ~ 10 mm. The relative densities of the samples were all found to be above 99%, except for the $x = 0.1$ sample with a relative density estimated at 98%. The second series of samples were prepared by the same technique of melting, quenching, annealing and sintering, using shots of Bi and Te (99.999%, 5N+), doped with chromium and Ga (99.99%, Sigma-Aldrich) pieces, and sintered in the same conditions.

2.2. Materials characterizations

Phase purity and crystal structure of sintered samples were characterised by powder X-ray diffraction (PXRD) using a Rigaku SmartLab 3 diffractometer (Cu $K_{\alpha 1}$ and $K_{\alpha 2}$ radiations, without monochromator) in reflection mode. The lattice parameters were determined by Rietveld refinement of the collected spectra using the FullProf program.

The microstructure and chemical composition of samples were characterized using a JEOL JSM-7001F field emission gun scanning electron microscope (SEM), equipped with energy-dispersive spectroscopy (EDS) and Oxford Instruments X-Max SSD detector. The obtained data were processed using the Aztec analytical software suite. The samples were prepared by polishing to a quarter of micron final finish.

2.3. Magnetic measurements

The magnetic susceptibility was measured on a Quantum Design MPMS-1T magnetometer at a field of 1,000 Oe at the temperature range of 4–300 K. Approximately 40 mg pieces of samples were loaded in a gelatine capsule for measurement.

2.4. Transport property measurements

The electronic transport properties of samples were measured in directions both parallel and perpendicular to the pressing direction in SPS. Bar-shaped samples ($\sim 2 \times 2 \times 8 \text{ mm}^3$) were cut to measure the electrical resistivity and the thermopower from room temperature to 523 K. These two measurements were carried out simultaneously using a ZEM-5 apparatus, Ulvac-Riko.

Thermal diffusivity was determined from room temperature to 523 K by using a Laser Flash Analyser (LFA 467-Netzsch) under argon flow on disk-shaped samples (~ 10 mm in diameter) for the parallel direction and on square prism-shaped samples ($\sim 6 \times 6 \times 1 \text{ mm}$) for the perpendicular direction. The thermal diffusivity of the nominal Bi_2Te_3 sample was only measured for parallel direction because of the lack of appropriate sample size. However, Thermal Transport Option (TTO) of a Quantum Design Physical Property Measurement System (PPMS) was adopted to determine the thermal conductivity of the Bi_2Te_3 sample in the perpendicular direction between 300 and 375 K. The thermal conductivity is calculated by $\kappa = d \cdot C_p \cdot \rho_v$ where d , C_p and ρ_v are the thermal diffusivity, mass heat capacity and density, respectively. A pyroceram disk was used as a reference to measure the heat capacity of samples according to the ASTM E 1461-07 method using LFA 467 Netzsch. Several previous reports [29,30] adopted the following equation to determine the specific heat capacity for similar samples: $C_p = 108.61 + 1.92 \cdot 10^{-2} \cdot T \text{ J} \cdot \text{mol}^{-1} \cdot \text{K}^{-1}$ [31]. This equation shows a very good approximation to our experimental data at temperatures above 450 K, however, underestimated the C_p values by $\sim 10\%$ at around room temperatures. The combined uncertainty in the determination of the zT values is estimated to be $\sim 17\%$ [32].

Bar-shaped samples cut in the perpendicular direction ($\sim 2 \times 2 \times 8 \text{ mm}^3$) were only used to obtain the Hall coefficient, R_H , from measurement of the transverse electrical resistivity with the AC transport option of a Quantum Design PPMS, in a five-wire configuration and under magnetic field ranging from ± 3 T, between 10 and 350 K. The Hall carrier concentration, n_H , was calculated using $n = 1/R_H \cdot e$. The low temperature transport properties of the sample $x = 0, 0.01$ and 0.02 were measured between 4 and 390 K on a sample of the same shape, using the TTO option of a Quantum Design PPMS. The measurement was used to probe the temperature dependence of the electronic mobility for these three samples.

2.5. Electronic structure calculations

The present total energy pseudopotential calculations were based on generalized gradient approximation parametrized by Perdew et al. [33,34] for the exchange-correlation in the density functional theory (DFT) [35,36]. The cut-off energies of 30 Ry for the wave functions and 300 Ry for the electron density were used. The crystal structure of Bi_2Te_3 is rhombohedral, and we used a corresponding hexagonal unit cell for $\text{Bi}_5\text{Cr}_1\text{Te}_9$ as $3(\text{Bi}_{1.667}\text{Cr}_{0.333}\text{Te}_3)$ and $\text{Bi}_{23}\text{Cr}_1\text{Te}_{36}$ as $12(\text{Bi}_{1.917}\text{Cr}_{0.083}\text{Te}_3)$ to simplify the calculation. Although $x = 0.333$ and $x = 0.0833$ contain quite high concentrations of Cr, they are qualitatively reproducible for experimental results. The lattice constants were fixed to the experimentally measured values. Internal atomic positions were structurally

optimized in their crystal symmetry with considering van der Waals (VdW) interactions using DFT-D3 [37,38]. The spin-orbit interaction was considered through the fully relativistic form of the atomic pseudopotentials [39] in the calculations. The calculations throughout this study were performed with Quantum Espresso code [40].

3. Structural analyses

The pseudo-binary $(\text{Bi,Sb})_2(\text{Se,Te})_3$ systems are layered narrow band gap semiconductors crystallizing in a rhombohedral unit cell. These compounds remain to date the most efficient thermoelectric materials for around room temperature applications [3] and harbour topological insulating properties, and they are the most extensively studied materials in the field [41–44]. In particular, the effect of transition metals on the topological insulating properties of bismuth chalcogenides was thoroughly studied, giving insight of their transport properties [45–48]. In addition, the solubility of 3d metal ions and their charge upon substitution for the pnictogen in Bi/Sb chalcogenides was theoretically estimated [49]. Fig. 1 shows the PXRD pattern of the sample $\text{Bi}_{1.99}\text{Cr}_{0.01}\text{Te}_3$. All patterns are indexed to the rhombohedral tetradymite structure of space group $R\bar{3}m$, (schematically shown in Fig. 1 inset). This structure consists of five planes of Te1–Bi–Te2–Bi–Te1, separated by VdW gaps. The PXRD data of all samples and the relevant lattice parameters obtained from Rietveld refinements of XRD spectra are included in Fig. S1 and Table S1 of Supplementary Information, respectively. The sample with $x = 0.1$ contains small additional peaks, indicating a minor impurity phase.

All XRD patterns are Rietveld refined to precisely determine the lattice parameters. A slight preferred orientation is detected in the samples because of structural anisotropy, and the lattice constants ($a = 4.3849 \text{ \AA}$ and $c = 30.481 \text{ \AA}$) are consistent with the values reported in literature [3,50]. Both lattice parameters of a and c are shown as a function of Cr concentration (x) in Fig. 2.

Although the variations of both a and c with x are small, for the sample with $x = 0.01$, the decrease in a departs from the general trend. Doping of 3d metals, such as Cr, Fe Mn or Cu, in this structure [45,47,51–53] indicates two possibilities: the direct substitution of Bi by the metal atoms or the intercalation in the VdW gaps, located between the two Te2–Te2 layers. The decrease in a exhibited by the $x = 0.01$ compound strongly suggests direct substitution of Cr for Bi, owing to the smaller size of the Cr^{3+} ion compared to covalently bonded Bi^{3+} . This substitution is expected to shrink the Bi layers

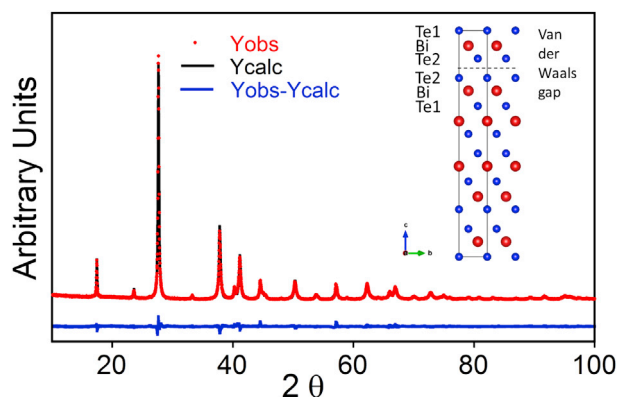


Fig. 1. Rietveld analysis of the X-ray diffraction pattern obtained from the sample $\text{Bi}_{1.99}\text{Cr}_{0.01}\text{Te}_3$. No significant anisotropy could be observed. Crystal structure of the Bi_2Te_3 compound projected along the a -axis; inset figure shows Bi and Te atoms by red and blue spheres, respectively.

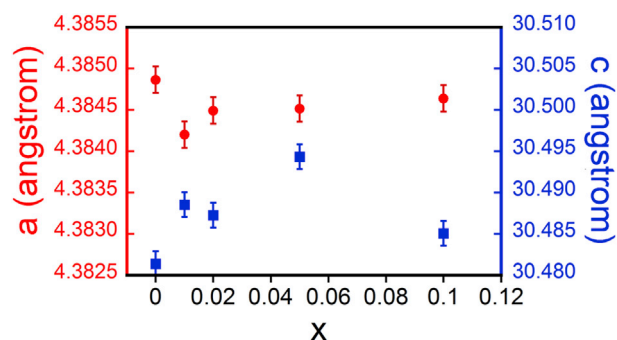


Fig. 2. Variation of the lattice parameters of $\text{Bi}_{2-x}\text{Cr}_x\text{Te}_3$ samples ($x = 0, 0.01, 0.02, 0.05$ and 0.10). Error bars on both a and c were estimated from the Rietveld refinements.

without affecting strongly the interlayer distances. This feature is, however, not shared with the other compounds, that should theoretically show a decrease in a . These samples have lower a values than the undoped sample; however, no further decrease is observed with x , suggesting a partial substitution of Cr for Bi and the presence of either Cr-based secondary phase or intercalation of Cr in the VdW gaps. On the other hand, the expansion of the c parameter for the sample $x = 0.05$ suggests that Cr ions are intercalated within the gaps. The SEM and EDS analyses of these samples have indicated the presence of Cr–Te–based precipitates for samples with $x > 0.02$. This is detailed in the Supplementary Information.

4. Electronic structure calculations

The electronic structure calculations were performed for Bi_6Te_9 , $\text{Bi}_5\text{Cr}_1\text{Te}_9$ and $\text{Bi}_{23}\text{Cr}_1\text{Te}_{36}$, and their total and projected densities of states are shown in Fig. 3. In this study, we considered the paramagnetic phase for $\text{Bi}_5\text{Cr}_1\text{Te}_9$ and $\text{Bi}_{23}\text{Cr}_1\text{Te}_{36}$ in order to evaluate the experimental results above the transition temperature as shown in Fig. 4, although the spin polarized phase is more favourable [49]. The Cr dopant concentrations in the calculation are $x = 0.333$ for $\text{Bi}_5\text{Cr}_1\text{Te}_9$ and $x = 0.0833$ for $\text{Bi}_{23}\text{Cr}_1\text{Te}_{36}$, respectively. These values are higher than concentrations of Cr in our compounds, however, because there is very little hybridization between the 3d states of Cr and the 5p and 6p states of Te and Bi [54], and our conclusions remain valid for samples with lower dopant levels. In Cr-doped systems, the partially filled Cr 3d levels are pinned at the Fermi level because of its paramagnetism; however, the contribution of Cr 3d levels around the Fermi levels decreases and has little effect on the energy distribution of the DOS as its concentration is reduced, leading to the conservation of the n-type degenerate semiconducting character.

5. Magnetic properties

Fig. 4(a) shows the temperature dependence of the magnetization (M) for $\text{Bi}_{2-x}\text{Cr}_x\text{Te}_3$ ($x = 0.01, 0.02, 0.05$ and 0.10) compounds, calculated per Cr atom, and the inverse molar magnetic susceptibility, χ^{-1} , between 5 and 300 K temperature range. All samples exhibit ferromagnetic ordering at low temperature. At the high temperature paramagnetic regime, inverse magnetic susceptibilities χ^{-1} were fitted using the Curie–Weiss law after correction for the diamagnetic contribution:

$$\chi = \frac{C}{T - \theta} + A \quad (1)$$

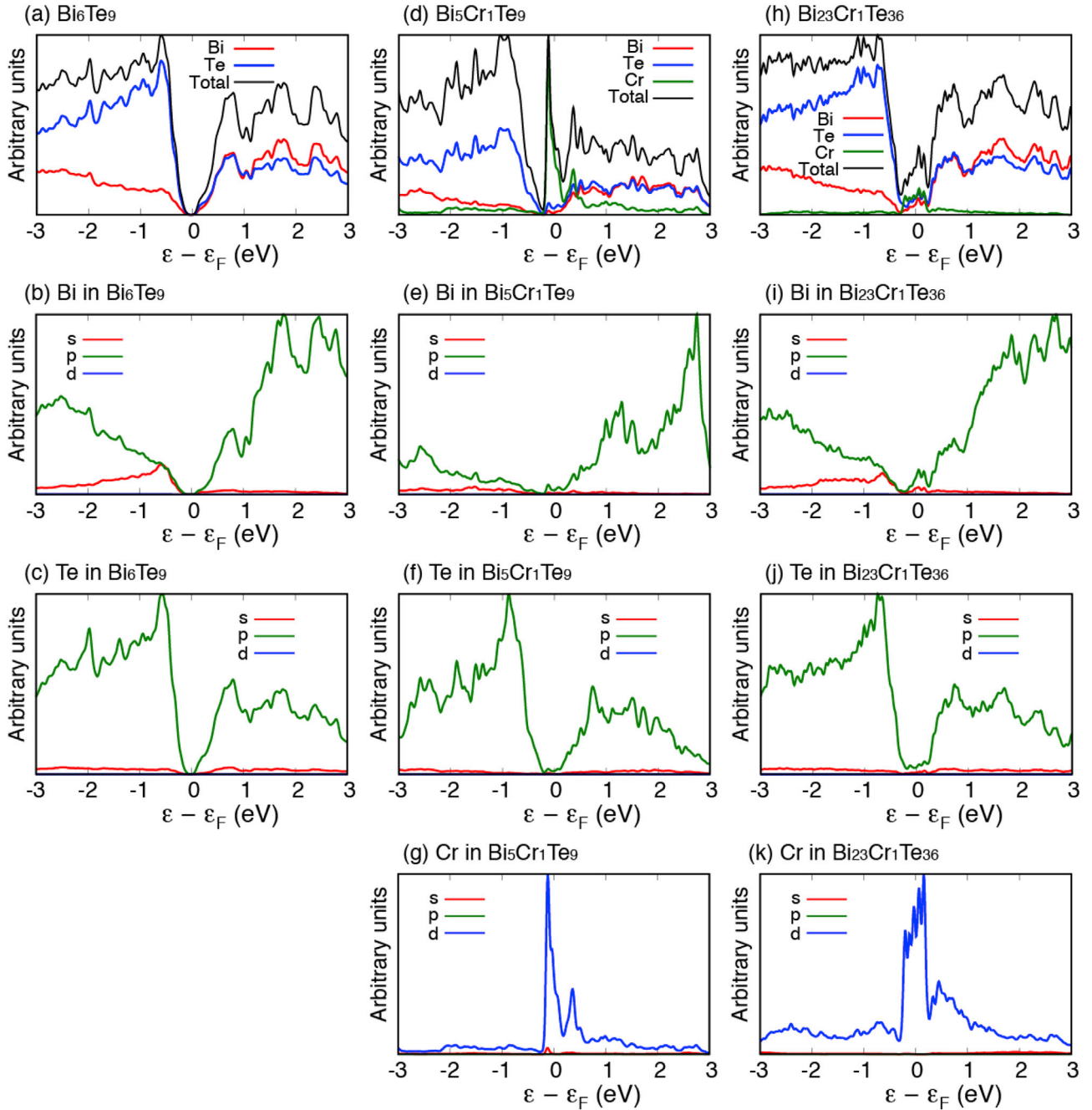


Fig. 3. The total and projected densities of states to each atomic element around the Fermi level of (a)–(c) Bi_6Te_9 , (d)–(g) $\text{Bi}_5\text{Cr}_1\text{Te}_9$ and (h)–(k) $\text{Bi}_{23}\text{Cr}_1\text{Te}_{36}$ are drawn, respectively. In the figures (b), (c), (e)–(g) and (i)–(k), the projected densities of states are resolved to each angular momentum.

where C is the Curie constant and $C = \frac{N_A \mu_{\text{eff}}^2}{3k_B}$ and A is the diamagnetic contribution, with N_A the Avogadro constant, k_B the Boltzmann constant and μ_{eff} the effective magnetic moment of the Cr atoms in the paramagnetic state, and θ is the Weiss constant and gives an indication of the magnetic interaction. θ Parameters were found to be positive and roughly constant for all x values, ranging between 217 K and 225 K without apparent trend. These values are considerably higher than those found for Mn–, Fe– or V-doped bismuth telluride (all below 50 K) [51,55–58], Cr-doping in bismuth selenide thin films (≈ 10 K) [46,59] and Cr intercalated TiTe_2 compounds (100–150 K) [60]. Higher values of θ , above 300 K, could only be observed in Cr-doped Bi_2Te_3 nanotubes, for which a strong influence of surface effects can be expected [61]. The values

of θ determined for our samples are similar to the temperature where the magnetization shows an abrupt uprise, indicative of ferromagnetic ordering. This is further supported by the field dependence of the magnetization, $M - H$ curves of $\text{Bi}_{1.99}\text{Cr}_{0.01}\text{Te}_3$ plotted for different temperatures in Fig. 4(b). The $M - H$ curve at 200 K indicates a ferromagnetic component, whereas it is almost linear at 300 K, consistent with the indicated temperature of the magnetic ordering. Such a high temperature ferromagnetic ordering has never been observed previously in bulk tetradymite and might have applications in the field of topological insulators.

The calculated effective magnetic moments provide very different values of μ_B for all values of x (Fig. 4). Comparing these values with values expected for different oxidation states,

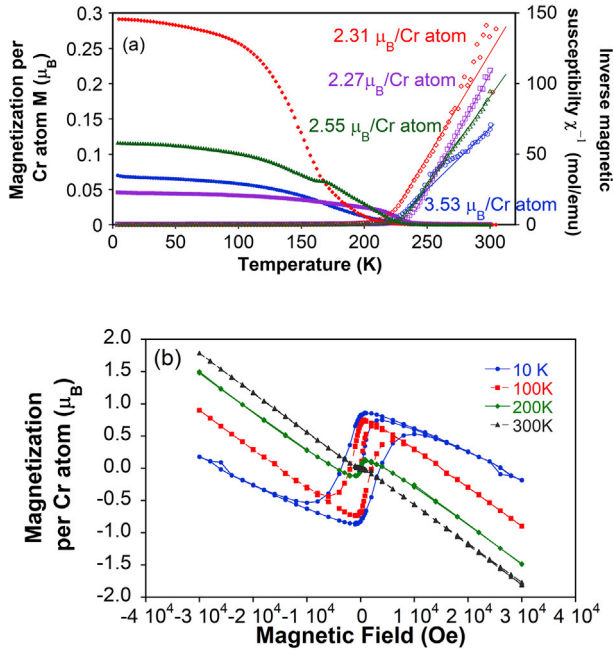


Fig. 4. (a) Low-temperature magnetic properties of the compounds $\text{Bi}_{2-x}\text{Cr}_x\text{Te}_3$ for $x = 0.01, 0.02, 0.05$ and 0.1 : magnetization per Cr atom (filled symbols) and inverse magnetic susceptibility (open symbols), after diamagnetic corrections; (b) field dependence of the magnetization, M – H curves of $\text{Bi}_{1.99}\text{Cr}_{0.01}\text{Te}_3$ at 10 K, 100 K, 200 K and 300 K.

summarized in Table 1, allows us to obtain an insight into the oxidation state and the coordination environment of the Cr ions. For $x = 0.01$, an effective magnetic moment of $3.53 \mu_B$ suggests an octahedral coordination and charge of $+3$, which is consistent with the aforementioned direct and neutral substitution of Cr for Bi, estimated from the XRD data and expected from theoretical calculations for n -type Bi_2Te_3 [49]. A small hump in χ^{-1} at 260 K departs from the classic linear Curie–Weiss law (even by taking into account the correction for the diamagnetic contribution). This might originate from the induced polarization of Bi and Te atoms or in some short-range ordering on a narrow temperature range. The evolution of the magnetic susceptibility and variations of the Cr atoms magnetic moment as a function of total Cr content is discussed in details in the Supplementary Information.

Although ferromagnetic ordering is observed for all samples at low temperatures, the average magnetization per Cr atom strongly depends on the concentration and occupation of the substitutional or interstitial sites by Cr atoms. In diluted magnetic semiconductors, the ferromagnetic exchange is carrier mediated according to the Ruderman–Kittel–Kasuya–Yoshida coupling mechanism [62]. Therefore, the variations in magnetization of Cr ions should also be understood in terms of differences in carrier mobilities and concentrations between samples.

Table 1
Magnetic moments of Cr ions calculated and observed depending on the oxidation state [71].

Cr ion oxidation state	$\mu_{\text{calculated spin-only}} (\mu_B)$	$\mu_{\text{observed}} (\mu_B)$
+2 Low spin state (octahedral)	2.83	3.2–3.3
+2 High spin state (octahedral)	4.90	4.7–4.9
+3 (Octahedral)	3.88	3.7–3.9
+4 (Tetrahedral)	2.83	2.6–2.8
+5 (Tetrahedral)	1.73	1.7–1.8

6. Electronic transport properties

6.1. 300–527 K electronic transport properties

The electrical resistivity ρ , Seebeck coefficient, S , and power factor S^2/ρ of $\text{Bi}_{2-x}\text{Cr}_x\text{Te}_3$ ($x = 0, 0.01, 0.02, 0.05$ and 0.10) samples are shown in Fig. 5 between 340 K and 523 K. Measurements were performed in both parallel and perpendicular to the pressing direction, except for $x = 0$ sample, for which only the perpendicular direction could be measured. For all samples and directions, the electrical resistivity exhibits typical metallic temperature dependence behaviour, indicative of the degenerate semiconducting

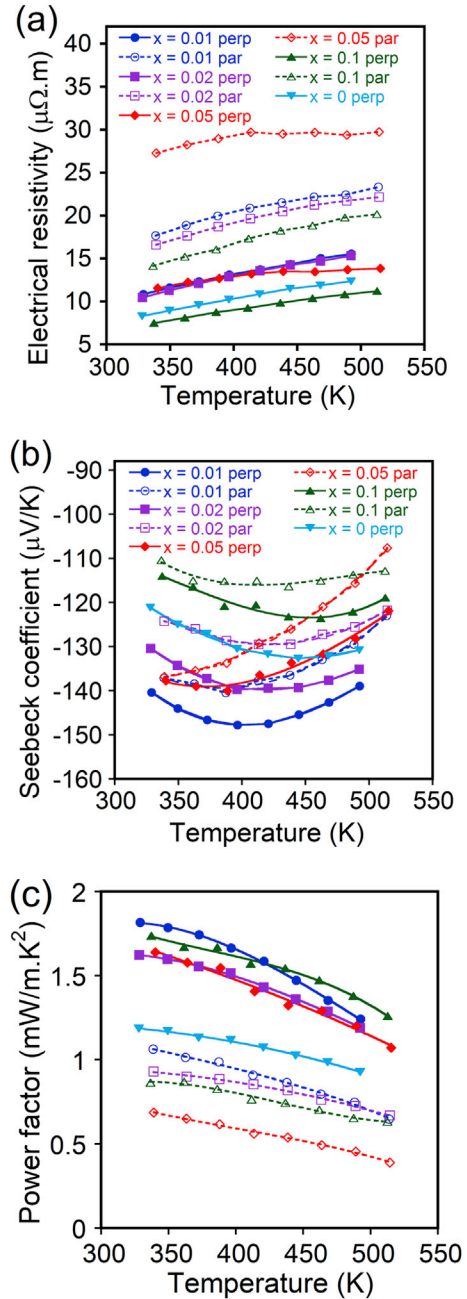


Fig. 5. The temperature dependence of (a) the electrical resistivity; (b) thermopower and (c) power factor for samples of $\text{Bi}_{2-x}\text{Cr}_x\text{Te}_3$ ($x = 0, 0.01, 0.02, 0.05$ and 0.1) for both directions, perpendicular to pressing (filled symbols) and parallel to pressing (open symbols) between 325 and 523 K.

nature of the samples. Despite moderate structural anisotropy observed from the XRD patterns, ρ shows a significant anisotropy for all compounds, with values of $\rho_{\text{perp}}/\rho_{\text{par}}$ ranging from 1.5 to 2.5, which is well known for n-type bismuth telluride alloys [63]. The change in anisotropy with x values can mostly be understood in light of the Cr atoms filling the VdW gaps, which increases the distance between the five plane layers. However, the presence of precipitates and their alignment along the grain boundaries, as evidenced in Fig. S2 of Supplementary Information, may also contribute to the anisotropy observed in the electronic transport properties of these samples. This results in a more pronounced confinement of the electronic transport within the layers in the a crystallographic direction; hence, more contrast is detected in the electrical conduction properties between the two directions. This effect is more apparent for the $x = 0.05$ sample, for which Cr intercalation is expected to be maximum in the series. Electrical resistivity, ρ , initially increases upon Cr substitution from $8.9 \mu\Omega \text{ m}$ at 350 K for the nominal compound up to $11.6 \mu\Omega \text{ m}$ for $\text{Bi}_{1.99}\text{Cr}_{0.01}\text{Te}_3$. The electrical resistivity then decreases for all compounds to $7.8 \mu\Omega \text{ m}$ for the $x = 0.1$ composite sample. The low resistivity for this sample might originate from the presence of the Cr–Te secondary phase, leading to the off-stoichiometry of the matrix Bi_2Te_3 phase.

The thermopower values (Fig. 5(b)) at room temperature are negative for all samples, indicative of electrons as the dominant charge carriers. Excess Te and associated defects (antisite substitution of Te for Bi–Te_{Bi}) are responsible for n-type conduction in Bi_2Te_3 [64,65]. All compounds of the present study show a maximum in thermopower within the range of 390–460 K, indicating a bipolar effect that is typical behaviour of thermoelectric degenerate semiconductors with narrow band gaps [66,67]. This phenomenon derives from the excitation of intrinsic carriers, competing with the extrinsic carriers, and decreasing Seebeck coefficient, S , with increasing temperature as a result of combined positive and negative charge carrier contributions. The highest values at 350 K are obtained for the $x = 0.01$ sample with a thermopower of $-144 \mu\text{V K}^{-1}$, a significant increase from the pristine compound which only shows a value of $-124 \mu\text{V K}^{-1}$ at this temperature. Above $x = 0.01$, thermopower decreases in absolute value for all samples without a clear trend. For all samples, the thermopower shows a small anisotropy between the measurements along the directions parallel and perpendicular to the pressing direction.

The power factors (Fig. 5(c)) show maximum values at 325 K for all samples, ranging from 1.62 to $1.82 \text{ mW m}^{-1} \text{ K}^{-2}$ in the perpendicular direction, which are considerably lower than the ones obtained in the parallel direction, owing to higher cross-plane electrical resistivity. The highest power factor of $1.82 \text{ mW m}^{-1} \text{ K}^{-2}$ is obtained in $\text{Bi}_{1.99}\text{Cr}_{0.01}\text{Te}_3$ at 325 K.

To confirm these findings, another series of Cr-doped Bi_2Te_3 were prepared with chromium concentrations of $x = 0.005$ and 0.01 . Ga-doped samples of $\text{Bi}_{2-y}\text{Ga}_y\text{Te}_3$ ($y = 0.01$ and 0.02) were also synthesised to compare substitution of non-magnetic univalent Ga^{3+} ions for Bi^{3+} ions with magnetic Cr^{3+} ions. The electrical resistivity, the thermopower and the power factor of these samples, measured perpendicular to the pressing direction, are shown in Fig. 6(a)–(c), respectively. The observed magnetic effect still appears for the Cr-doped samples, while the corresponding Ga-doped samples show no increase in the absolute value of the Seebeck coefficient. Fig. 6(c) shows that the power factors significantly increase for the latter Cr-doped samples, whereas no improvement is observed for the Ga-doped counterparts. These values do not, however, exceed the power factors previously measured for the first set of samples. This is most likely due to higher carrier concentrations in these samples.

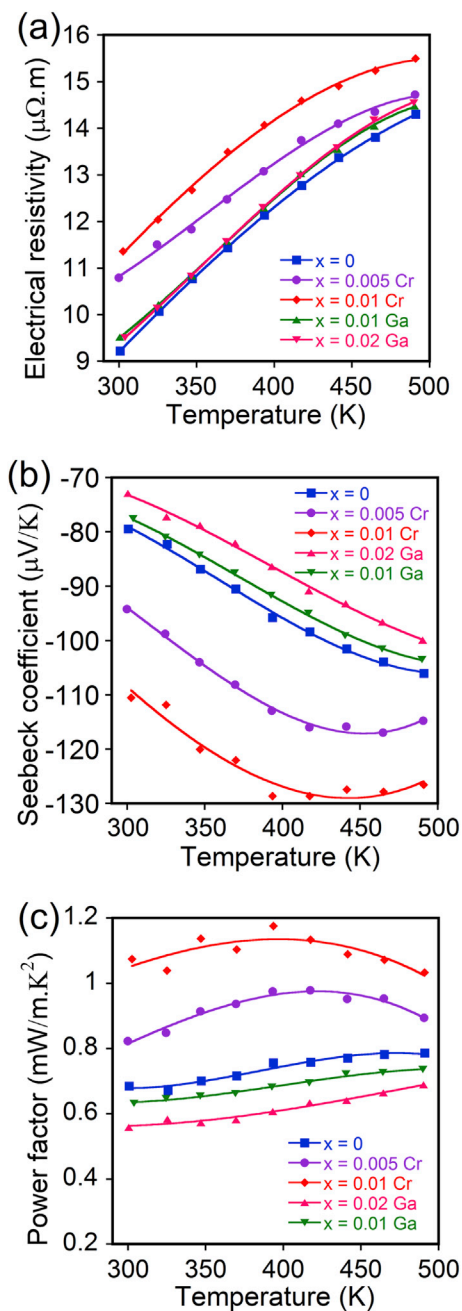


Fig. 6. Temperature dependence between 300 and 523 K of (a) the electrical resistivity; (b) thermopower and (c) power factor for compounds $\text{Bi}_{2-x}\text{D}_x\text{Te}_3$ for D = Cr, Ga and $x = 0, 0.005, 0.01$ and 0.02 , perpendicular to the pressing direction.

6.2. Carrier concentration and transport analysis

The electronic transport properties of all samples perpendicular to pressing direction at 350 K are summarised in Table 2. The temperature dependence of the Hall carrier concentration, $n = 1/eR_H$, was calculated between 5 and 350 K from the Hall coefficient, R_H , and plotted in Fig. S3 of the Supplementary Information. It is worth noting that the Hall coefficient is a tensor, and we have measured the Hall coefficient, only perpendicular to the pressing direction. The Hall coefficients are all negative, consistent with the n-type conduction, evidenced from the thermopower measurements. The carrier concentration of all samples, n , is above $3.5 \times 10^{19} \text{ cm}^{-3}$, whereas n-type Bi_2Te_3 -based systems usually harbour optimal thermoelectric performance at carrier

Table 2The electronic transport properties of $\text{Bi}_{2-x}\text{Cr}_x\text{Te}_3$ ($x = 0, 0.01, 0.02, 0.05$ and 0.10) samples, perpendicular to the direction of pressing at 350 K.

Cr content (x)	Thermopower S ($\mu\text{V.K}^{-1}$)	Carrier concentration n (10^{19} cm^{-3})	Electronic mobility, μ_H ($\text{cm}^2.\text{V}^{-1}.\text{s}^{-1}$)	Calculated carrier effective mass m^* (m_0)	Cr atoms effective magnetic moment (μ_B)
0.00	−124	5.70	123	0.71	—
0.01	−144	5.74	94.0	0.87	3.53
0.02	−134	5.00	111	0.72	2.27
0.05	−136	6.00	85.4	0.83	2.31
0.1	−115	4.69	169	0.57	2.55

concentration in the lower range of 10^{19} cm^{-3} [3,53]. These rather high charge carrier densities suggest the presence of a large number of charged structural defects. The measured carrier concentrations were found to be almost the same for the entire temperature range for both undoped and $x = 0.01$ as predicted by theoretical calculations [49], which is in line with our aim of probing the sole effect of magnetism on the transport properties. However, for samples with higher Cr content, carrier concentration varies significantly, initially decreases with increasing x from 0.01 to 0.02. This might be associated with the reduction of Cr^{3+} into Cr^{2+} for $\text{Bi}_{1.98}\text{Cr}_{0.02}\text{Te}_3$, or with the intercalation of the dopant in the VdW gaps. The effect of ionic 3d metal dopants intercalation on the number of carriers is not straightforward, and 3d metal dopants can act as both donors and acceptors similar to Ti dichalcogenides [60,68]. For $\text{Bi}_{1.98}\text{Cr}_{0.02}\text{Te}_3$ sample, the change in temperature dependence at $\approx 200 \text{ K}$ could be the result of magnetic ordering on the electronic transport properties; however, no similar effect is evidenced for the other compounds. In addition, the Hall resistivity curves versus applied magnetic field are plotted in Fig. S4 of the Supplementary Information. Anomalous Hall effect is observed below the Curie temperature, whereas at the paramagnetic phase, the Hall resistance varies linearly with the magnetic field.

As already predicted theoretically [49], the substitution of 3d metals in Bi_2Te_3 is highly dependent on the carrier type and the nominal carrier concentration, i.e. on the defects concentration inherent to the fabrication process. Further work is, therefore, needed to verify the possibility of such neutral substitutions with 3d elements on both n- and p-type, for various compounds and a broad range of properties.

The Hall mobilities, μ_H , were calculated at 350 K using $\mu_H = 1/n.e\rho$ and summarised in Table 2. To gain an understanding of the interaction between charge carriers and the magnetic dopant elements, the effective mass of carriers, m^* , was calculated from the measured Seebeck coefficients, S , and carrier concentration, n , assuming a single parabolic band structure, in the absence of phonon drag effect and energy-independent scattering [69], using the following equations:

$$S = \pm \frac{k_B}{e} \left[\xi_F - \frac{r + 5/2}{r + 3/2} \frac{F_{r+3/2}(\xi_F)}{F_{r+1/2}(\xi_F)} \right] \quad (2)$$

$$n = \frac{4\pi(2k_B m_0 m^*)^{3/2}}{h^3} F_{1/2}(\xi_F) \quad (3)$$

where k_B is the Boltzmann constant, e the electron charge, m_0 the electron mass, ξ_F the reduced Fermi energy and r the scattering parameter. $F_i(\xi_F)$ is the Fermi function, defined as

$$F_i(\xi_F) = \int_0^\infty \frac{x^i dx}{1 + e^{(x-\xi_F)}} \quad (4)$$

The scattering parameter, r , was evaluated from the temperature dependence of the Hall mobilities, μ_H , according to $\mu_H = \mu_0 T^{r-1}$,

assuming acoustic scattering as the dominant scattering process. Although the value of r close to the room temperature is usually assumed to be -0.5 for acoustic scattering only, the fitting of μ_H between 200 and 350 K gave a slightly higher value of -0.26 , suggesting mixed acoustic and ionized impurity scattering [69], consistent with values measured at room temperature for Fe-doped Bi_2Se_3 [70]. The effective masses are summarised in Table 2. Although the single parabolic band model does not precisely describe the electronic properties of a degenerate multivalley semiconductors such as Bi_2Te_3 , it provides a reasonably good approximation of the effective mass, m^* , to compare samples with roughly similar electronic band structure.

The most interesting results obtained from the effective masses is the net increase of m^* from $0.71 m_0$ to $0.87 m_0$ upon doping Cr at 1% mol on the Bi site at roughly constant carrier concentration. The effective mass of the undoped compound was found to be within the same range as other n-type Bi_2Te_3 compounds with similar carrier concentrations. The weighted mobility μ_w can be defined as

$$\mu_w = \mu \left(\frac{m^*}{m_0} \right)^{3/2}. \quad (5)$$

It includes the contributions of both the electron mobility and the effective mass in a single parameter and, therefore, can be considered as a quality criterion for the charge transport in thermoelectric materials. This parameter increases from $73.6 \text{ cm}^2 \text{ V}^{-1} \text{ s}^{-1}$ to $76.3 \text{ cm}^2 \text{ V}^{-1} \text{ s}^{-1}$ with Cr substitution at $x = 0.01$ and then decreases for all other compounds. This increase, although small, sheds light on the underlying mechanism of carrier–magnetic moment coupling, eventually resulting in an increase in thermopower apart from other well-known strategies. It is worth noting that the presence of magnetic impurities deteriorates the carrier mobility (evidenced in Table 2), and therefore, the weighted mobility is enhanced slightly. We attribute the slight increase in the power factor of $\text{Bi}_{1.99}\text{Cr}_{0.01}\text{Te}_3$ than that of Bi_2Te_3 to the increase in μ_w , highlighting further the interest of utilizing magnetic interactions in thermoelectric materials. If heavier charge neutral Cr-doping on the Bi site alone is possible, the effect should also be magnified, giving rise to further enhanced power factor.

For the second series of samples, n , μ and m^* were also calculated and summarised in Table S1. In order to obtain a broader and therefore more clear vision of the obtained data, the Seebeck coefficient was plotted as a function of n for all samples (Fig. 7) and compared with the values obtained from the SPB model for a constant effective mass of $0.72 m_0$. For the undoped and Ga-doped samples, S values are in good agreement with those expected for an effective mass of $m^* = 0.72 m_0$. On the other hand, the values of S for the Cr-doped samples lie significantly higher than the expected values for this effective mass, except for the samples doped at concentrations above $x = 0.02$, for which large amounts of chromium telluride secondary phases were detected. In the latest set of samples, m^* increases from $0.73 m_0$ to $0.97 m_0$ upon substitution of $x = 0.01$ Cr. But more strikingly, the weighted mobility increases μ_w from $34.8 \text{ cm}^2 \text{ V}^{-1} \text{ s}^{-1}$ to $50.9 \text{ cm}^2 \text{ V}^{-1} \text{ s}^{-1}$. These values, however, do not exceed those measured for lower carrier concentration samples but unambiguously demonstrate the effect of magnetic doping on the thermoelectric properties. The larger magnitude of

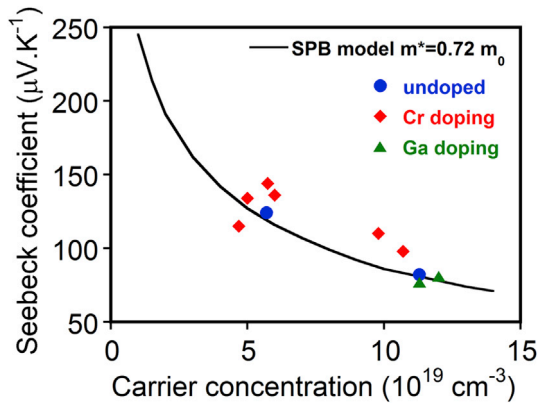


Fig. 7. Absolute value of the Seebeck coefficient as a function of the carrier concentration n for the undoped, Cr-doped and Ga-doped samples, with the Seebeck values estimated from the SPB model for an effective mass of $m^* = 0.72 m_0$. SPB, single parabolic band.

this effect at higher carrier concentration is not well understood yet and should be the subject of further studies. Notably, it may be of interest to dope samples with magnetic elements in compounds for which the optimized zT values lie at high carrier concentration.

6.3. Low-temperature electronic transport properties (5 K–300 K)

Fig. 8(a) and (b) show the electrical resistivity and Seebeck coefficient of Bi_2Te_3 and $\text{Bi}_{1.99}\text{Cr}_{0.01}\text{Te}_3$ samples between 5 and 300 K. The temperature dependence of the electrical resistivity clearly shows a discontinuity and a change in slope at the ferromagnetic–paramagnetic transition temperature. In the ferromagnetic phase, the 3d levels of Cr are split below and above the Fermi level (for majority and minority spins, respectively), hence results in no significant effect on the electrical transport. However, in the paramagnetic phase, the 3d levels of Cr lie directly at the Fermi level E_F as shown in Fig. 3, resulting ultimately in the change of the slope. Interestingly, the Seebeck coefficient remains unaffected by the magnetic transition. With the 3d levels of Cr lying very close to E_F , their contribution to S is very small (it basically scales to $\frac{E - E_F}{k_B T}$ for each state). The relatively small number of these states results only in a negligible contribution to the thermopower, therefore no changes observed in S at the transition temperature.

Higher dopant levels on the same site should, however, result in a visible change.

In addition, the absence of a discontinuity in S at the magnetic transition totally rules out the effect of resonant states. For resonant doping, an effect can be observed when resonant electronic states lie at E_F . However, for the present study samples, Cr 3d states lie only at E_F in the paramagnetic state and split away from it in the ferromagnetic region. This consequently would result in a higher S in the paramagnetic region, and a discontinuity of S could be observed at T_C .

It is also worth noting that the Seebeck coefficient value is determined by two parameters: one depending solely on the band structure and the density of states near E_F and the other stemming from the effects of scattering mechanisms, including scattering by magnetic impurities [3]. This discontinuity of the thermopower indicates that the magnetic enhancement of S indeed might not originate from the former contribution but rather from the scattering mechanism and therefore through the effect of the magnetic moments on the motion of the electrons.

7. Thermal properties and figure of merit zT

The temperature dependence of the total thermal conductivity, κ , between 300 and 523 K for all samples of $\text{Bi}_{2-x}\text{Cr}_x\text{Te}_3$ is presented in Fig. 9(a). All samples show significant anisotropy between the measurements for perpendicular and parallel to the pressing direction, with small variations with x . Except for the undoped Bi_2Te_3 compound that shows a minimum around 375 K, all other samples exhibit a monotonic increase with temperature. Comparably low values in the range of $1\text{--}1.5 \text{ W m}^{-1} \text{ K}^{-1}$ at 300 K were obtained parallel to the pressing direction, while measurements perpendicular to pressing direction showed values up to $2.2 \text{ W m}^{-1} \text{ K}^{-1}$ in the undoped compound at 300 K. More details about the thermal behaviour of these samples are provided in the [Supplementary Information](#).

The figure of merit, zT , was calculated between 300 and 532 K for all samples for the first set of samples and presented in Fig. 9(b). The highest value of the figure of merit, ~ 0.4 , was obtained at 375–400 K for the sample $\text{Bi}_{1.99}\text{Cr}_{0.01}\text{Te}_3$. Although lower zT are generally obtained for n-type Bi_2Te_3 compared to p-type Bi_2Te_3 , the low thermoelectric efficiency of our samples is associated with the lack of carrier concentration optimization. We also purposely sintered at the lowest SPS temperature which provided us with samples with relative density of over 98%. Sintering at high

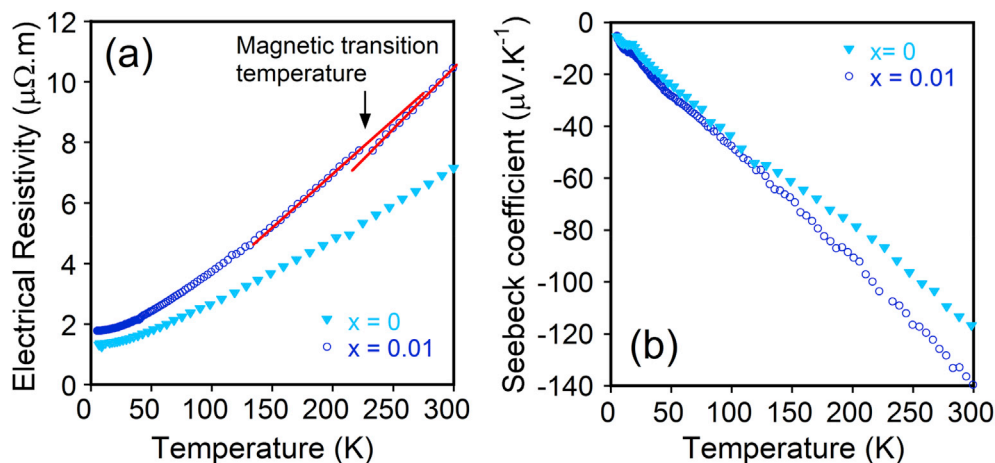


Fig. 8. Temperature dependences of the electrical resistivity (a) and Seebeck coefficient (b) between 5 and 300 K, for Bi_2Te_3 and $\text{Bi}_{1.99}\text{Cr}_{0.01}\text{Te}_3$ samples, having the same carrier concentrations.

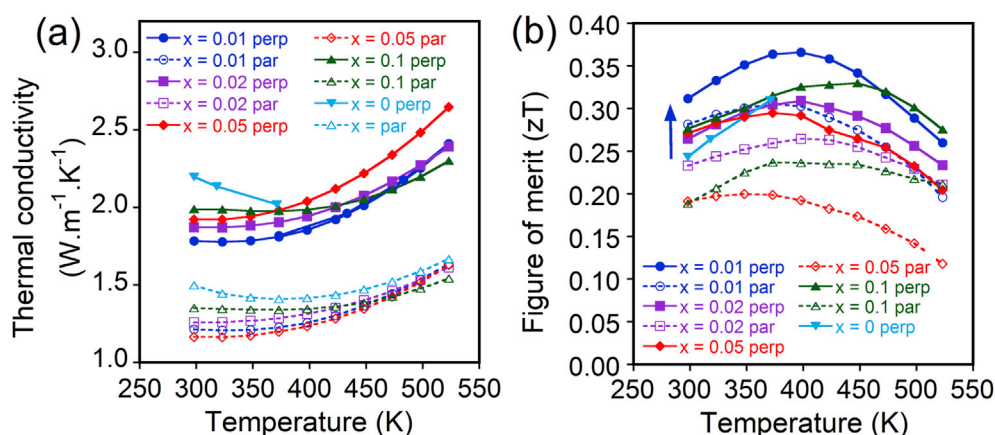


Fig. 9. Temperature dependence of (a) the thermal conductivity and (b) the figure of merit (zT) between 300 and 523 K for $\text{Bi}_{2-x}\text{Cr}_x\text{Te}_3$ ($x = 0, 0.01, 0.02, 0.05$ and 0.10) samples.

temperatures can result in inhomogeneity of Bi_2Te_3 samples in terms of composition and introduces defects which both effect on the electronic transport properties, and may lead to one-off high zT , but which may also not be stable in long-term applications at high temperatures. The highest zT values for n-type Bi_2Te_3 -based compounds (~ 1) are achieved in nanostructured Bi_2Te_3 - Bi_2Se_3 alloys at optimised carrier concentrations, doped with Cu, which is also an element with magnetic moment. The aim of this study was to decouple the effect of magnetism and the carrier concentration-related effect to prove the importance of magnetism on thermoelectricity; this was not viable to achieve in complex chemistries, and therefore, we demonstrated the magnetic enhancement effect in this way. Nevertheless, with $x = 0.01$, the figure of merit shows an increase of roughly 25% compared to the undoped compound, at constant carrier concentration. The magnetic doping, leading to magnetic interaction with the carriers driving the increased S and leading to decreased κ_{latt} , due to the point defect scattering, results in the observed enhancement in zT . For the other compounds, the slight variations of n and the loss of the magnetic coupling of the carriers due to intercalation of the Cr ions prevent samples to achieve higher values of zT .

8. Conclusion

The substitution of Cr for Bi in the state-of-art thermoelectric bismuth telluride has been studied. We demonstrated the possibility of isovalent substitution of Cr for Bi, keeping the carrier concentration roughly constant up to $x = 0.01$ and decoupling the carrier concentration and magnetic scattering effects on the thermopower. The increase in effective mass leads to an enhanced thermopower and consequently a higher power factor. Together with a reduction of the thermal conductivity due to the enhanced point defect scattering and likely increased anharmonicity this results in 25% enhancement in the zT value of the undoped compound. However, limited solubility of Cr substitution in bismuth telluride and intercalation in the VdW gaps prevented us to probe this effect further.

The magnetic doping, which led to magnetic interaction with the carriers, was shown to be an efficient method to improve the thermoelectric performance of Bi_2Te_3 compounds, at fixed carrier concentration. This method could make its way into the already rich toolbox of the scientist studying thermoelectricity and becomes a standard strategy for improving the performance of thermoelectric materials. One large advantage of this method over phenomenon such as magnon drag is that magnetic interaction is present in the same magnitude at higher temperatures, above the

transition temperature (i.e. the transition temperature is simply manifested because of a competition with magnetic interaction and thermal excitation). Therefore, its effects on the carrier transport can lead to enhanced thermoelectric properties at high temperatures, and thus, this thermoelectric enhancement effect is quite robust. It is even very likely that this effect is already at play in thermoelectric materials containing magnetic elements but masked by the contribution of the changes in charge carrier concentration.

In addition, we observed high ferromagnetic ordering at temperatures > 200 K obtained in the bulk sample, which very favourably compares to other 3d metals substitutions in Bi_2Te_3 and might give new insights towards the experimental realization of topological insulators in this family of compounds.

Data availability

The raw/processed data required to reproduce these findings cannot be shared at this time because of technical or time limitations.

Acknowledgements

Support from JST CREST Grant Number JPMJCR15Q6, Japan is thanked. JSPS KAKENHI JP17H02749, JP16F16706, JP16H06441 is also acknowledged. J.B.V. is supported by a JSPS Fellowship. Philipp Sauterschnig is thanked for help with the magnetization measurements. This work was supported by an Australian Research Council (ARC) Discovery Early Career Research Award (DE130100310).

Appendix A Supplementary data

Supplementary data to this article can be found online at <https://doi.org/10.1016/j.mtphys.2019.03.004>.

References

- [1] X. Zhou, et al., *Mater. Today* 21 (9) (2018) 974.
- [2] J.R. Sootsman, et al., *Angew Chem. Int. Ed. Engl.* 48 (46) (2009) 8616.
- [3] D.M. Rowe, *Thermoelectrics Handbook: Macro to Nano*, CRC press, 2006.
- [4] E.S. Toberer, et al., *Chem. Mater.* 22 (3) (2009) 624.
- [5] D.T. Morelli, et al., *Phys. Rev. Lett.* 101 (3) (2008) 035901.
- [6] B.C. Sales, et al., *Science* 272 (5266) (1996) 1325.
- [7] T. Mori, *Small* 13 (45) (2017) 1702013.
- [8] K. Biswas, et al., *Nature* 489 (2012) 414.
- [9] J. He, et al., *Mater. Today* 16 (5) (2013) 166.
- [10] A.U. Khan, et al., *Nano Energy* 31 (2017) 152.
- [11] S. Aminoroaya Yamini, et al., *ACS Appl. Mater. Interfaces* 6 (14) (2014) 11476.
- [12] S. Aminoroaya Yamini, et al., *Adv. Energy Mater.* 5 (21) (2015) 1501047.

- [13] H.J. Goldsmid, *Materials* 7 (4) (2014) 2577.
- [14] J.P. Heremans, et al., *Science* 321 (5888) (2008) 554.
- [15] J.P. Heremans, et al., *Energy Environ. Sci.* 5 (2) (2012) 5510.
- [16] Y. Pei, et al., *Adv. Mater.* 23 (47) (2011) 5674.
- [17] Y. Lee, et al., *J. Am. Chem. Soc.* 135 (13) (2013) 5152.
- [18] K. Ahn, et al., *Energy Environ. Sci.* 6 (5) (2013) 1529.
- [19] Y. Tang, et al., *Nat. Mater.* 14 (12) (2015) 1223.
- [20] Y. Pei, et al., *NPG Asia Mater.* 4 (2012) e28.
- [21] L.M. Rogers, A.J. Crocker, *J. Phys. D Appl. Phys.* 4 (7) (1971) 1016.
- [22] S. Aminorroaya Yamini, et al., *Phys. Chem. Chem. Phys.* 16 (5) (2014) 1835.
- [23] M. Zabarjadi, et al., *Nano Lett.* 11 (6) (2011) 2225.
- [24] N. Tsujii, T. Mori, *APEX* 6 (4) (2013) 043001.
- [25] R. Ang, et al., *Angew. Chem., Int. Ed. Engl.* 54 (44) (2015) 12909.
- [26] F. Ahmed, et al., *J. Mater. Chem. A* 5 (2017) 7545.
- [27] N. Tsujii, et al., *Sci. Adv.* 5 (2019) eaat5935.
- [28] H. Takaki, *Mater. Today Phys.* 3 (2017) 85.
- [29] M. Hong, et al., *ACS Nano* 10 (4) (2016) 4719.
- [30] M. Hong, et al., *Nano Energy* 20 (2016) 144.
- [31] K.C. Mills, *Thermodynamic Data for Inorganic Sulphides, Selenides and Tellurides*, Butterworths, United Kingdom, 1974.
- [32] E. Alleno, et al., *Rev. Sci. Instrum.* 86 (1) (2015) 011301.
- [33] J.P. Perdew, et al., *Phys. Rev. Lett.* 78 (7) (1997) 1396.
- [34] J.P. Perdew, et al., *Phys. Rev. Lett.* 77 (18) (1996) 3865.
- [35] W. Kohn, L.J. Sham, *Phys. Rev.* 140 (4A) (1965) 1133.
- [36] P. Hohenberg, W. Kohn, *Phys. Rev.* 136 (3B) (1964) 864.
- [37] S. Grimme, et al., *J. Chem. Phys.* 132 (15) (2010) 154104.
- [38] S. Grimme, et al., *J. Comput. Chem.* 32 (7) (2011) 1456.
- [39] A. Dal Corso, *Comput. Mater. Sci.* 95 (2014) 337.
- [40] G. Paolo, et al., *J. Phys. Condens. Matter* 21 (39) (2009) 395502.
- [41] L. Fu, C.L. Kane, *Phys. Rev. B* 76 (4) (2007) 045302.
- [42] Y.L. Chen, et al., *Science* 325 (5937) (2009) 178.
- [43] D. Hsieh, et al., *Phys. Rev. Lett.* 103 (14) (2009) 146401.
- [44] Y. Xia, et al., *Nat. Phys.* 5 (6) (2009) 398.
- [45] Y.S. Hor, et al., *Phys. Rev. Lett.* 104 (5) (2010) 057001.
- [46] P.P.J. Haazen, et al., *Appl. Phys. Lett.* 100 (8) (2012) 082404.
- [47] V.K. Maurya, S. Patnaik, *AIP Conference Proceedings* 1591 (2014) 1239.
- [48] K. Carva, et al., *Phys. Rev. B* 93 (21) (2016) 214409.
- [49] J.-M. Zhang, et al., *Phys. Rev. B* 88 (23) (2013) 235131.
- [50] G.R. Miller, et al., *J. Appl. Phys.* 34 (5) (1963) 1398.
- [51] V. Kul'bachinskii, et al., *J. Exp. Theor. Phys. Lett.* 73 (7) (2001) 352.
- [52] M.-K. Han, et al., *J. Electron. Mater.* 42 (9) (2013) 2758.
- [53] K.H. Lee, et al., *J. Mater. Chem. C* 3 (40) (2015) 10604.
- [54] P. Larson, W.R.L. Lambrecht, *Phys. Rev. B* 78 (19) (2008) 195207.
- [55] J. Choi, et al., *Phys. Status Solidi B* 241 (7) (2004) 1541.
- [56] Z. Zhou, et al., *Appl. Phys. Lett.* 88 (19) (2006) 192502.
- [57] N.H. Jo, et al., *Phys. Rev. B* 87 (20) (2013) 201105.
- [58] J.S. Lee, et al., *Phys. Rev. B* 89 (17) (2014) 174425.
- [59] L.J. Collins-McIntyre, et al., *EPL (Europhysics Letters)* 107 (5) (2014) 57009.
- [60] N.V. Baranov, et al., *J. Phys. Condens. Matter* 21 (50) (2009) 506002.
- [61] M. Kim, J.-H. Song, *J. Appl. Phys.* 111 (7) (2012) 07E307.
- [62] M.A. Ruderman, C. Kittel, *Phys. Rev.* 96 (1) (1954) 99.
- [63] R.T. Delves, et al., *Proc. Phys. Soc.* 78 (5) (1961) 838.
- [64] J. Horák, et al., *Phil. Mag. B* 69 (1) (1994) 31.
- [65] J. Fleurial, et al., *J. Phys. Chem. Solids* 49 (10) (1988) 1237.
- [66] Z.M. Gibbs, et al., *Appl. Phys. Lett.* 106 (2) (2015) 022112.
- [67] H.J. Goldsmid, J.W. Sharp, *J. Electron. Mater.* 28 (7) (1999) 869.
- [68] A.V. Postnikov, et al., *Comput. Mater. Sci.* 17 (2) (2000) 450.
- [69] G.S. Nolas, et al., *Thermoelectrics: Basic Principles and New Materials Developments*, Springer Berlin Heidelberg, 2001.
- [70] V.A. Kulbachinskii, et al., *J. Magn. Magn. Mater.* 272–276 (2004) 1991.
- [71] J.M.D. Coey, *Magnetism and Magnetic Materials*, Cambridge University Press, 2010.